BNL-114419-2017-JA

A new strategy to engineer polymer bulk heterojunction solar cells with thick active layers via self-assembly of tertiary columnar phase

H. Li, C-Y. Nam

Submitted to the Journal of Nanoscale

July 2017

Center for Functional Nanomaterials

Brookhaven National Laboratory

U.S. Department of Energy
USDOE Office of Science (SC),
Basic Energy Sciences (BES) (SC-22)

Notice: This manuscript has been authored by employees of Brookhaven Science Associates, LLC under Contract No. DE- SC0012704 with the U.S. Department of Energy. The publisher by accepting the manuscript for publication acknowledges that the United States Government retains a non-exclusive, paid-up, irrevocable, world-wide license to publish or reproduce the published form of this manuscript, or allow others to do so, for United States Government purposes.

DISCLAIMER

This report was prepared as an account of work sponsored by an agency of the United States Government. Neither the United States Government nor any agency thereof, nor any of their employees, nor any of their contractors, subcontractors, or their employees, makes any warranty, express or implied, or assumes any legal liability or responsibility for the accuracy, completeness, or any third party's use or the results of such use of any information, apparatus, product, or process disclosed, or represents that its use would not infringe privately owned rights. Reference herein to any specific commercial product, process, or service by trade name, trademark, manufacturer, or otherwise, does not necessarily constitute or imply its endorsement, recommendation, or favoring by the United States Government or any agency thereof or its contractors or subcontractors. The views and opinions of authors expressed herein do not necessarily state or reflect those of the United States Government or any agency thereof.

A new strategy to engineer polymer bulk heterojunction solar cells with thick active layers via self-assembly of tertiary columnar phase

Hongfei Li,[a] Zhenhua Yang,[a] Cheng Pan,[a] Naisheng Jiang,[a] Sushil K. Satija,[b] Di Xu,[a] Dilip Gersappe,[a] Chang-Yong Nam,[*,c] and Miriam H. Rafailovich [*a]

[a]Department of Materials Science and Engineering, Stony Brook University, Stony Brook, New York 11794, United States

[b]Center for Neutron Research, National Institute of Standards and Technology, Gaithersburg, Maryland 20899, United States.

[c]Center for Functional Nanomaterials, Brookhaven National Laboratory, Upton, New York 11973, United States

[*]E-mail: miriam.rafailovich@stonybrook.edu (M.H.R.), cynam@bnl.gov (C.-Y.N)

Abstract

We report that the addition of a non-photoactive tertiary polymer phase in the binary bulk heterojunction (BHJ) polymer solar cell leads to the self-assembled columnar nanostructure, enhancing charge mobilities and photovoltaic efficiency with surprisingly increased optimal active blend thicknesses over 300 nm, 3-4 times larger than that of the binary counterpart. Using the prototypical poly(3-hexylthiophene) (P3HT):fullerene blend as a model BHJ system, we discover that the inert poly(methyl methacrylate) (PMMA) added in the binary BHJ blend self-assembles into vertical columns, which not only template the phase segregation of electron acceptor fullerenes but also induce the out-of-plane rotation of the edge-on-orientated crystalline P3HT phase. Using complementary interrogation methods including neutron reflectivity, X-ray scattering, atomic force microscopy, transmission electron microscopy, and molecular dynamics simulations, we show that the enhanced charge transport originates from the more randomized molecular stacking of P3HT phase and the spontaneous segregation of fullerenes at the P3HT/PMMA interface, driven by the high surface tension between the two polymeric components. The results demonstrate a potential method for increasing the thicknesses of high-performance polymer BHJ solar cells with improved photovoltaic efficiency, alleviating the burden of stringently controlling the ultrathin blend thickness during the roll-to-roll-type large-area manufacturing environment.

Introduction

Organic polymer solar cells, especially those based on bulk heterojunction (BHJ) structure, have generated extensive interests in the past decades due to their mechanical flexibility, solution processibility, and potentially lower manufacturing costs.[1] Typically, BHJ solar cells consist of binary blend thin films, where a photoactive polymer is mixed with a fullerene-based electron acceptor, and the exciton dissociation occurs along the interfaces generated between the two components.[2] Owing to the advances in material development and associated device engineering, the best BHJ solar cell efficiency has surpassed 10%.[3-5] However, this high efficiency, achieved in small-scale devices, has not been readily translated into high performances of the BHJ solar cells fabricated by the large-area fabrication methods such as the roll-to-roll (R2R) or slot-die coating, which generally leads to considerably lower device efficiencies (<5%).[6,7]

One of the practical issues of the large-area fabrication method is that typical high-performance organic BHJ blend solar cells have sub-100 nm optimal active layer thicknesses, and the uniform coating of such ultrathin organic BHJ blend layers by these large-area coating technologies is non-trivial. Instead, much thicker layer thicknesses, for instance over 300 nm, are preferable in order to fabricate uniform active BHJ blend layers without pin-holes and defects that cause dysfunctional devices.[8,9] In general, the high photovoltaic performance, particularly the photocurrent output, of BHJ solar cells requires the increased amount of photons absorbed by the active blend layer and the high mobility of free charge carriers in the active layer for efficient collection of free charge carriers.[10,11] In principle, the improvement in photon absorption can be achieved by simply increasing the active layer thickness for a given system, but because of the typically low charge mobility inside the active BHJ layer, the increased active layer thickness over the usual optimal value (<~100 nm) does not yield an improved photocurrent output but rather was found to reduce the photovoltaic parameters and overall performance.[12,13] The issue is especially prevalent in most of the state of the art low band gap polymers, as their optimal BHJ blend layer thicknesses tend to be <80 nm.[14] Fundamentally, the low charge mobility is in part caused by the nanoscale phase-separated morphology in the active BHJ layer, which creates long circuitous pathways for charge transport, rendering the free charge carriers more prone to the recombination loss.[15-17]

It is thus recognized that the improvement in the charge carrier collection in the BHJ blend layer is critical not only for improving the overall solar cell efficiency but also for realizing an increased device optimal thickness, desired for the reliable large-area device fabrication. While the earlier studies for improving the charge transport and collection have been focused on optimizing the nanoscale BHJ morphology by, for instance, varying the polymer:fullerene blend ratio and thermal or solvent annealing condition,[18-20] there have been efforts exploring the development of an ordered BHJ structure, which in concept consists of well-defined, phase-separated p- and n-type regions with straight charge transport pathways toward electrodes.[21,22] Many

studies related with the latter approach have reported the use of micro- or nanolithography to create template patterns onto substrates, which then could be filled by photoactive components. Despite some successes in achieving improved device performance, these methods are time consuming and expensive to apply, and often shown to be ineffective,[23] due to the improper segregation of electron acceptors in the template structures or the radical groups on the template surface, which results in an undesirable charge recombination before their extraction to electrodes.[24,25] Furthermore, these approaches could not increase the optimal blend layer thickness beyond the typical optimal values.

In a separate branch of research efforts, several groups have postulated that the performance enhancement in the BHJ solar cell could be achieved by introducing a tertiary polymer phase into the binary BHJ, creating ternary blend BHJ solar cells. One of the first studies, reported by Bazan group, has demonstrated an enhanced PV efficiency of polymer:fullerene binary BHJ solar cells by adding less than one percent of high-molecular-weight photo-inactive polystyrene as an additive for optimizing the BHJ morphology.[26] More recent works have focused on adding photoactive tertiary polymer components, which not only improved the morphology of the active blend layer,[27-29] resulting in an enhanced charge transport,[30, 31] but also expanded the solar spectral coverage compared with the original binary blend.[31-34] Nevertheless, these methods were also still limited by the diminishing efficiency when the blend layer thickness was increased over 100 nm.[30-31, 35-36] In our previous work, we showed that another factor potentially applicable for improving the performance of ternary blend BHJ solar cells was the self-assembly of ordered columnar structure consisting of an inert tertiary phase which templated more efficient pathways for extracting free charge carriers to the electrodes.[37,38]

In this study, we report that the self-assembled inert tertiary columnar polymer phase added to the polymer:fullerene binary BHJ solar cells enables a significantly increased optimal polymer BHJ solar cell thickness, which was accompanied by an improved device photovoltaic performance, compared with the binary control device. We apply our ternary blend scheme on a model binary blend system, the archetypical poly(3-hexylthiophene) (P3HT):phenyl-C_{61}-butyric acid methyl ester (PCBM) BHJ solar cell. When a non-photoactive poly(methyl methacrylate) (PMMA) is blended in the binary P3HT:PCBM BHJ, the champion power conversion efficiency (PCE) of ternary blend devices reaches near 4% at the optimal ternary blend layer thickness over 300 nm, despite that ~40% of the ternary blend is the photo-inactive PMMA. By combining complementary neutron reflectivity and X-ray scattering measurements, atomic force microscopy, transmission electron microscopy, molecular dynamics simulation, and device electrical and photovoltaic characterization, we identify that the large surface tension between the two polymeric components, P3HT and PMMA, induces the self-assembly of vertical PMMA columnar domains and the spontaneous segregation of PCBM layer at the P3HT/PMMA interface. These result in the increased electron and hole mobilites through

the BHJ device and eventually enhanced P3HT:PCBM blend phase material photovoltaic performance with much thicker optimal active layer thickness. The finding demonstrates a potential method for improving the material charge transport properties in existing photovoltaic BHJ materials and, consequently, increasing their optimal device thicknesses to make them more suitable for the large-area, R2R-type mass manufacturing.

Experimental section

Neutron reflectivity

The neutron reflectivity experiments were performed with the NG7 reflectometer at the Cold Neutron Facility of the National Institute of Standards and Technology (Gaithersburg, MD) with a wavelength (λ) of 4.76 Å and $\Delta\lambda/\lambda$ ~0.025. First, approximately 30 nm P3HT thin film was spin-cast onto a 5 mm thick polished silicon wafer treated by a 5 % hydrofluoric acid solution. Then, approximately 40 nm deuterated PMMA (dPMMA) thin film was floated off on the surface of the deionized water bath. Finally, we picked up the floating film by the substrate covered by P3HT layer in the water bath. 50 wt. % PCBM was added into the top or bottom layer (in the solution phase before spin-coating) to investigate the diffusion and aggregation of PCBM in the polymer bilayer matrix. X-ray reflectivity measurements were applied prior to neutron reflectivity experiments to measure the thicknesses of bilayer samples.

Grazing incidence wide angle X-ray scattering (GIWAXS) measurement

GIWAXS measurements for binary and ternary blend thin films were carried out at the X9 beamline (λ = 0.0918 nm (13.5 keV)) at the National Synchrotron Light Source (NSLS), Brookhaven National Laboratory. Two-dimensional scattering patterns were collected using a MAR-CCD area detector. The incident angle (α) of 0.18° was used to investigate the structure information of the thin film. All the results were collected at room temperature under vacuum. The X-ray exposure time of 120 s was used for all the measurement.

Conducting atomic force microscopy (AFM)

The conductivity mapping measurements of the ternary blend active layer were conducted using an atomic force microscope (Bruker Dimension Icon). The P3HT:PMMA:PCBM ternary blend solution (1:1:1 wt. ratio, in chlorobenzene) was spin-coated on a Si wafer or indium tin oxide (ITO)-coated glass substrate further coated with a 30 nm thick TiO_2 layer prepared by spin-casting a precursor solution and annealing at 400 °C for

2 hr on a hot plate in air ambient. The TiO_2 precursor solution was prepared by the sol-gel method: 10 ml of tetrabutyl titanate was first dissolved in 100 ml of ethanol, followed by the sequential addition of acetic acid (10 ml), acetylacetone (10 ml), and de-ionized water (10 ml). The mixture was stirred at room temperature for 30 min. The conductivity mapping data was obtained by using a peak-force tunnelling (PF-TUNA) module (1 nN peak force, 2 V DC bias, Au-coated Si AFM tip with spring constant of 0.4 N/m).

Transmission electron microscopy (TEM) characterization

To prepare the cross-sectional TEM sample, the P3HT:PMMA:PCBM ternary blend thin films were prepared on a silicon wafer first by spin-coating. Then, focused ion beam (FIB) lift-out technique was used to prepare the cross-sectional TEM sample (FEI Helios FIB). All the TEM images were taken under 80 kV (JEOL 1400).

Solar cell fabrication and photovoltaic characterization

ITO-coated glass substrates were treated in ultraviolet (UV)-ozone for 10 min. Then, around 50 nm-thick poly (3, 4-ethylenedioxythiophene):polystyrene sulfonate (PEDOT:PSS) layer was spin-coated on the ITO substrate at 5000 rpm for 45 s. The substrate was baked on a hot plate at 140 °C, followed by spin-coating the binary or ternary polymer blend solution (20 mg/ml, 1:1 or 1:1:1 wt. ratio in chlorobenzene) in ambient air. Spin speed was varied from 700 rpm to 3000 rpm to achieve different film thicknesses. A 70 nm-thick Al top contact was deposited by thermal evaporation at pressure lower than 3×10^{-7} Pa. The fabricated devices were annealed at 150 °C for 1 hr in ~10 mTorr vacuum. The device photovoltaic characteristics were measured under 1 Sun air mass 1.5 global (AM1.5G) illumination condition (set by a calibrated Si solar cell standard (Newport)) in ambient air on a modified probe station equipped with 150 W solar simulator (Oriel) and a precision semiconductor parameter analyzer (Agilent).

Hole- and electron only device fabrication for mobility measurement

For the hole-only device, the top Al contact of the solar cell was replaced by MoO_3 (8 nm)/Ag (90 nm), wherein MoO_3 acts as an electron blocking layer. The layers were deposited by thermal evaporation at pressure lower than 3×10^{-7} Pa. The fabricated devices were annealed at 150 °C for 1 hr in ~10 mTorr vacuum. For the electron-only device, the bottom PEDOT:PSS of the solar cell was replaced by TiO_2 (30 nm) deposited by spin-casting a TiO_2 sol-gel precursor solution and annealing at 400 °C for 2 hr on a hot plate in air ambient.

The current-voltage (I-V) characteristics of the fabricated devices were measured by a semiconductor parameter analyzer in a dark ambient-air condition using a probe station. The measured I-V characteristics were analysed by the space-charge-limited current (SCLC) model: $I = A\,(9/8)\,\mu\varepsilon_o\varepsilon_r V^2 L^{-3}$, where A is the device area, μ mobility, ε_o vacuum permittivity, ε_r semiconductor dielectric constant (~3), and L the blend layer thickness. From the slopes of the linear portions of $I\text{-}V^2$ plots, the corresponding μ values were determined.

Molecular dynamics simulations

We used a bead-spring model to simulate two immiscible polymers,[39] labelled as A (non-photoactive) and B (photoactive), confined in a thin film domain. Large-scale atomic/molecular massively parallel simulator (LAMMPS) package was used for our simulations. All the quantities in the simulation are reduced to a dimensionless format by setting energy unit ε, distance unit σ, and Boltzmann constant k_b to unity. Standard velocity-Verlet time integration was utilized with step length $\Delta t = 0.005\tau$, where τ is the time scale. To simulate the thin film geometry, particle walls were imposed to the top and bottom of simulation domain. Each wall, made of two layers of Lenard Jones spheres densely packed in (111) face-centered cubic lattice, moved as an entity. The other two dimensions (x and y) were periodic with fixed length of 60σ. The model simulates an isothermal–isobaric ensemble. The temperature is set to be unity by using a Nose-Hoover thermostat, and the pressure is controlled by slightly moving the top wall to adjust the internal pressure to be close to 0. The thickness of systems therefore can have small variations, but they were limited to 0.5σ as we observed in the simulations. The polymers had uniform length of 8 segments in our simulation and bonds were simulated by the finitely extensible nonlinear elastic (FENE) potential U^{FENE}:

$$U^{FENE} = 0.5R_0^2 k \ln\left[1 - \left(\frac{r}{R_0}\right)^2\right] \qquad (1)$$

, where R_0 is the maximum extensible length for the chemical bond (set to 1.5σ), and k is the spring constant (set to 30).[40] We used a fixed composition of 20% polymer A and 80% polymer B for all the simulations and adjusted the thickness by increase the total number of particles. All results presented were at simulation time = $1.5 \times 10^5\tau$.

Results and discussion

Photovoltaic performance of P3HT:PMMA:PCBM ternary blend BHJ solar cells

We tested the photovoltaic characteristics of P3HT:PMMA:PCBM ternary blend and P3HT:PCBM control binary blend BHJ solar cells and found that the addition of the tertiary PMMA phase significantly improved the material photovoltaic performance and enabled an increased optimal device active layer thickness. The tested device structure consists of ITO/PEDOT:PSS/P3HT:PMMA:PCBM (1:1:1 wt. ratio) or P3HT:PCBM (1:1 wt. ratio) blend/Al (see Experimental section for more details). Fig. 1a shows the representative J-V (J: Current density) characteristics for the champion ternary blend and control binary blend solar cells under 1 Sun (100 mW/cm^2), AM1.5G illumination condition, with corresponding photovoltaic parameters summarized in Table 1. The major performance enhancement with the addition of PMMA in the binary blend device arises from the increased apparent short circuit current density (J_{SC}) from ~8 mA/cm^2 to ~12 mA/cm^2, with power conversion efficiency (PCE) improving from 2.5% to 3.8% (c.f., open circuit voltage (V_{OC}) remains at ~0.6 V). More significantly, the optimal active layer thickness of the champion ternary blend device was much larger than that of the P3HT:PCBM binary blend device; Fig. 1b and Fig. 1c describe the variation of PCE and J_{SC} for the ternary and binary blend solar cells as a function of the active blend layer thickness. Clearly, PCE and J_{SC} of the control binary blend cell decrease rapidly with increasing film thickness beyond 100 nm (fill factor (FF) decreases similarly while the decrease in V_{OC} is relatively insignificant. See Tables S1 and S2). This trend has been well documented by several research groups and is ascribed to the increasing internal electrical resistance in the blend film and the consequently increased charge carrier recombination caused by the tortuosity of the phase-separated blend phases.[41-43] In contrast, the ternary blend solar cell overall has a higher apparent PCE, which peaks at the blend thickness between 300 nm and 400 nm. We note that another important factor that influences the blend-thickness-dependent J_{SC} and PCE is the optical inference effect caused by the reflection of incident light at the interfaces within the device stack and the top metal contact.[44] However, the variation in the light absorption becomes relatively small for the blend thickness beyond ~300 nm for the P3HT:PCBM device with identical contact structures as in the current study,[44] suggesting that the observed 'peaking' behavior of J_{SC} and PCE is mostly caused by the increasing internal electrical resistance. Nevertheless, the determination of precise optimal blend thickness will indeed require a data fitting that accounts for the optical inference within the device.

The enhanced PCE is remarkable considering that the ternary blend contains ~38% of non-photoactive PMMA and consequently has a ~40% lower measured optical absorption compared with the binary blend film of identical thickness (Fig. S1). The average J_{SC} of the ternary blend device normalized by the photoactive volume reaches 15.2 ± 0.7 mA/cm^2 as a result, which is slightly larger than what was previously observed in the P3HT:PCBM binary blend confined in cylindrical nanopores with conformal TiO_2 electron contact layer (14.6 mA/cm^2).[45] If the apparent J_{SC} is normalized by the photoactive volume, the corresponding PCE per volume of photoactive P3HT:PCBM in the ternary blend is reaching ~5.1% on average. Generally, the optimal

blend active layer thickness in BHJ solar cells is determined by the interplay between the amount of light absorption and the extent of free charge carrier recombination, both of which increase for a larger blend thickness. With increasing blend thickness, a significant charge recombination will dominate eventually, decreasing the device photovoltaic performance. The observed increase in optimal blend thickness with the addition of ternary PMMA phase suggests an improved charge collection efficiency through the photoactive P3HT:PCBM phase. A similar increase in the optimal blend thickness has been reported previously for P3HT:PCBM binary blend BHJ solar cells when carbon nanotubes were added as three-dimensional hole collecting electrodes in the device.[46]

Self-assembly of PMMA columnar domains and spontaneous segregation of PCBM at the P3HT/PMMA interface

The internal structure of the ternary blend film was investigated by combining AFM and TEM, and we identified the self-assembly of vertical PMMA columnar domains and the spontaneous segregation of PCBM layer at the P3HT/PMMA domain interface. We spin-cast P3HT:PMMA:PCBM solution (1:1:1 wt. ratio, in chlorobenzene) on PEDOT:PSS-coated ITO-glass substrate and examined the surface structure of the cast ternary blend film by AFM after subjecting the film to a 150 °C thermal annealing for 1 hr. The topographical and deformational AFM images shown in Fig. 2a and 2b reveal that there exist two major phase-separated domains, a more deformable continuous matrix and an imbedded spherical phase with higher mechanical rigidity. Given the much higher glass transition temperature (T_g) of PMMA (~100 °C) compared with that of P3HT (T_g~12 °C),[47] we deduce that the spherical domains are most likely PMMA. The diameter of spherical domains appears to have a bimodal distribution, the smaller ones with mean diameter ~0.75 μm and the larger with ~3 μm (Fig. 2c). The total areal fraction occupied by the spherical PMMA domains (conversely, volume fraction if the domains extend vertically from top to bottom) is approximately 38%, which, as discussed, translates into a reduced amount of light absorption compared with the binary blend film of identical thickness because PMMA is not photoactive (Fig. S1). We note that the AFM data indicate an appreciable height difference between PMMA domains and the P3HT:PCBM matrix, and even after the top metal contact deposition, this surface topography was transferred to the top (Fig. S2).

TEM study of the ternary blend thin film reveals that PCBM is predominantly segregated at the P3HT/PMMA interface, which is consistent with the neutron reflectivity measurements performed on layered control thin film samples as discussed later. The blend films were floated off from the ITO-glass substrate in water (by dissolving the PEDOT:PSS layer) and transferred onto TEM grids. Fig. 3a shows a representative bright-field TEM image, where the spherical PMMA phase displays a brighter contrast than the continuous

P3HT:PCBM blend matrix due to more significant beam damages on the PMMA phase. We notice prominent dark rings at the interface between the spherical PMMA domains and the P3HT matrix, regardless of the PMMA domain diameter. Considering the higher electron stopping power of PCBM compared with those of P3HT and PMMA,[48] we expect that these dark rings are mainly composed of PCBM. Cross-sectional TEM further shows that the spherical PMMA domains span over the whole thickness of the ternary blend film, forming three-dimensional cylindrical volume elements extending from the top air interface to the bottom substrate (Fig. 3b). The dark interfacial layer at the P3HT/PMMA interface is also observed again, delineating the segregated interfacial PCBM layer vertically extended throughout the blend thickness, which should serve as efficient and direct pathways for the electron conduction toward the electrode. The width of the interfacial layer (marked by two red solid lines in Fig. 3b) is estimated to be ~7 nm by measuring the difference of the contrast.

The described phase segregation information is further confirmed using the PF-TUNA AFM, where an electrically grounded ternary blend sample is locally biased by an Au-coated Si conducting AFM tip, and the relative magnitude of electrical currents through the sample is mapped across the surface. Fig. 4a shows a representative low-magnification conducting AFM image, where the continuous P3HT matrix clearly displays a higher current conduction (i.e., brighter in the color scheme) than the non-conductive spherical PMMA domains. In a higher resolution scan (Fig. 4b), highly conducting (bright) rings with width of ~8 nm are observed around the spherical PMMA domains regardless of their diameters, which is comparable to the thickness of PCBM interfacial layer observed in TEM. Since the smaller spherical domain has a longer perimeter per area than the larger domain, the contribution of interfacial PCBM layer around the smaller PMMA domains to the electron conduction per area should be more significant than that around the larger PMMA domains. From the diameter distribution we observed (Fig. 2c), we estimate that the smaller diameter domains (average diameter 0.75 μm) should contribute at least 60% to the total electron conduction, if excluding the electron conduction through the network of PCBM remaining in P3HT matrix.

Origin of self-assembly of PMMA columnar domains and spontaneous PCBM segregation

We study the fundamental phase separation behavior between P3HT, PMMA, and PCBM via the neutron reflectivity measurements on control bilayer thin film samples. The reflectivity data were fitted to the reflectivity profiles calculated from the model scattering length density (SLD) profiles via Parratt's Recursion method.[49] The fitting was performed using Levenberg−Marquardt nonlinear least-squares method by adjusting film thickness, SLD, and interfacial width (i.e., twice of the roughness of bottom layer) of the layers as fitting

parameters. Then, we could calculate the associated volume fraction profiles of each component phases by integrating the SLD profiles based on the same calculation method used in our previous work.[37]

Fig. 5a shows the neutron reflectivity data and corresponding best fits obtained from deuterated PMMA (dPMMA)/P3HT bilayer films without PCBM and with 50 wt. % PCBM in either dPMMA or P3HT after thermal annealing. Fig. 5b plots the resulting component volume fraction profiles for the dPMMA/P3HT bilayer case, which clearly indicate that the P3HT and PMMA are highly immiscible as they form a sharp interface with less than ~5 nm interfacial thickness upon spin-casting (top panel) and even after annealing at 150 °C for 90 min (bottom panel). When a dPMMA film with 50 wt. % PCBM was floated onto a pure P3HT layer (top panel) and annealed (bottom panel), the PCBM particles diffused into the P3HT layer, forming ~5 nm thick layers at the P3HT/dPMMA and Si/P3HT interfaces (Fig. 5c). When a dPMMA layer was floated onto a P3HT layer having 50 wt. % PCBM (Fig. 5d), two segregated PCBM layers spontaneously emerged even without annealing (top panel), one at the dPMMA/P3HT interface (~3.5 nm thick) and the other at the P3HT:Si interface (~5 nm). Meanwhile, we found no discernable diffusion of PCMB into the dPMMA layer even after thermal annealing (bottom panel). These results indicate that PCBM does not have an appreciable miscibility in PMMA and prefers the P3HT phase, which is consistent to what has been reported previously.[50-52] More importantly, the segregation of PCBM at the P3HT/PMMA interface, regardless of the initial conditions, suggests that the PCBM segregation is an equilibrium phenomenon that is expected to occur in the P3HT:PMMA:PCBM ternary blend.

Influence of PMMA columnar domains on the molecular structure of P3HT:PCBM blend

To study the potential influence of PMMA columnar domains on the molecular structural characteristics of P3HT:PCBM blend phase, we performed the GIWAXS measurements on the control P3HT:PCBM binary blend (Fig. 6a, left panel) as well as the P3HT:PMMA:PCBM ternary blend (Fig. 6a, right panel) thin films. In both cases, we observe up to the third order scattering peak corresponding to the "edge-on" P3HT lamellar stacking on the q_z axis (q_z = 1.15 Å^{-1}).[15, 52] Additionally, we find that the size of edge-on lamellar domain is nearly identical for both cases (~20 nm, calculated from the measured full-width at half maximum of scattering peaks (Fig. S3) using Scherrer equation.[53] See the details in Supplementary information). However, we notice that there is a depletion of PCBM from the P3HT:PVBM blend phase by the addition of PMMA—the X-ray scattering ring corresponding to a polycrystalline PCBM phase, whose intensity is proportional to the amount of PCBM in the matrix, [54, 55] is clearly visible in the control binary sample (Fig. 6a, left panel; q ~ 1.43 Å^{-1})[52, 56] but disappears completely for the ternary blend case (Fig. 6a, right panel). This indicates a significant depletion of PCBM from the P3HT:PCBM blend matrix upon the addition of PMMA because PCBM

preferentially segregates at the P3HT/PMMA interface. The absence of crystalline PCBM X-ray scattering signature, despite the visible presence of ~5 nm thick PCBM layer at the P3HT/PMMA interface, is most likely caused by the physical confinement that frustrates the PCBM crystallization; the PCBM domain size in the binary blend, calculated from the Scherrer equation, is ~9.9 nm. This is consistent to the typical values reported in previous studies (10-20 nm)[55, 57] but larger than our observed PCBM interfacial layer width between the PMMA columnar domains and P3HT matrix in the ternary blend sample. A closer examination of P3HT scattering feature also reveals the randomization of P3HT domain orientation. In Fig. 6b, we compare the angular intensity distribution of the scattering peak at q ~ 1.71 $Å^{-1}$, related with the "face-on" (i.e., π-π) P3HT lamellar stacking configuration,[52, 58] and find that the angular intensity distribution becomes nearly constant with the introduction of the tertiary PMMA phase. This implicates that the orientation of the face-on lamellar configuration becomes more randomized in the ternary blend film. In contrast, the angular distribution of the edge-on lamellar stacking peak (q ~ 1.15 $Å^{-1}$) virtually does not change by the addition of PMMA (Fig. 6c). This asymmetric impact of PMMA on the two different P3HT stacking orientations can be in part understood by the nearly immobile edge-on P3HT phase adjacent to the substrate due to its low interfacial energy, [59] which will hinder the lamellar reorientation upon the introduction of PMMA. Meanwhile, the P3HT phase in the middle portion of blend film has a higher fraction of face-on orientation,[55, 56, 60] which can be reoriented and randomized around the PMMA columnar domains in the ternary blend.

Charge transport in the ternary blend thin film

We determine the influence of the ternary blend structure on the charge transport parameters, in particular electron and hole mobilities, by fabricating and characterizing electron- and hole-only blend devices adopting carrier selective contacts (see Experimental section). In both devices, the trap-free space SCLC model was used to obtain the charge mobilities from the slopes of the linear portions of measured I-V^2 curves (Fig. 7a).[58, 61] We find that the measured average hole mobility is $4.5 \pm 0.2 \times 10^{-2}$ $cm^2V^{-1}s^{-1}$ in the ternary system, ~10 times higher than the mobility measured from the P3HT:PCBM binary blend control device ($3.1 \pm 0.24 \times 10^{-3}$ $cm^2V^{-1}s^{-1}$; both measured under ambient air) (Fig. 7b; Table 2). The average electron mobility of the ternary blend was found to be $8.4 \pm 0.35 \times 10^{-5}$ $cm^2V^{-1}s^{-1}$, ~2 times higher than that of the control devices, $4.6 \pm 0.35 \times 10^{-5}$ $cm^2V^{-1}s^{-1}$ (Fig. 7b; Table 2), which is in accordance with the previous result reported in a similar blend system.[38] We note this relatively large difference in hole and electron mobilities can cause unbalanced charge transports and may have been responsible for somewhat low FF values (<~0.53) observed in both the binary and ternary blend devices in the current study.

The hole mobility of semi-crystalline P3HT is well-known to be sensitive to the polymer crystallinity as well as molecular orientation. The enhancement of hole mobility has been previously reported in ternary systems, and its origin has been attributed to the change in the P3HT lamellar orientation from the edge-on to the face-on direction with respect to the substrate plane.[61-63] The hole mobility observed in our control binary blend sample is relatively high compared with the values reported in previous reports, which is consistent with the GIWAXS data displaying the presence of a large population of face-on P3HT configuration in the control binary blend (Fig. 6a, left panel).[60, 64] The addition of PMMA in the binary blend randomized the face-on P3HT lamellar orientation while resulting in insignificant changes in the size and orientation of edge-on P3HT lamellar domains as discussed, and this is in fact expected to alleviate the *grain boundary effect* and cause the increase in hole mobility: It has been shown that the misorientation between neighboring crystalline polymer domains (i.e., grains) could negatively affect the inter-grain charge transport.[65-68] Our control binary blend film had both highly ordered edge-on and face-on domains in the polymer matrix as confirmed by GIWAXS data, indicating a presence of highly misoriented (i.e., 90 degree) polymer domains. The tertiary PMMA phase induced an appreciable randomization of the face-on P3HT lamellar orientation, relaxing the domain misorientation with the edge-on phases, and this subsequently should be able to improve the hole transport across neighboring polymer domains.

Another factor that is likely to have contributed to the enhanced hole mobility in the ternary blend is the observed depletion of PCBM from the P3HT:PCBM blend matrix surrounding the columnar PMMA domains, induced by the spontaneous segregation of PCBM to the P3HT/PMMA interface. Specifically, the top-view AFM image of the ternary blend we discussed earlier (Fig. 2a) suggests that approximately 70 wt.% of PCBM is segregated along the perimeter of the PMMA columns, being removed from the P3HT:PCBM blend matrix (assuming ~5 nm interfacial PCBM width and vertically extending cylindrical PMMA domains; see Supplementary information). Previous studies have shown that the presence of PCBM in conjugated polymer:PCBM blends could reduce the hole mobility due to the increased bimolecular carrier recombination and more tortuous charge transport pathways along the polymer phase.[69,70] The presence of PCBM can also reduce the polymer crystallinity by hindering the long-range ordering of lamellar structures.[69,71] Meanwhile, the improved electron mobility can be attributed to the interfacial PCBM segregation on the columnar PMMA domains as it provides shortened pathways vertically traversing the film thickness for direct electron transport toward the electrode.

The above discussed structural characteristics enable us to deduce the structural configuration of individual components within the P3HT:PMMA:PCBM ternary blend thin film (Fig. 7c). First, the tertiary PMMA self-assembles into vertical columns extending from the bottom to the top of the ternary blend film and

imparts influences on the structures of P3HT and PCBM—the orientation of the P3HT lamellar domains predominantly stays immobilized as edge-on at the bottom substrate surface but becomes more randomized toward the upper portion of the film, most likely driven by the interaction between P3HT and the self-assembled PMMA vertical columns, which becomes stronger away from the bottom surface. This is the primary factor that increases the hole mobility. The vertical PMMA columns also induce the depletion of PCBM from the P3HT:PCBM binary blend matrix and the segregation of PCBM on the surface of PMMA columns with the segregation layer thickness of ~5 nm, which frustrates the PCBM crystallization. The segregated surface PCBM domain extends across the ternary blend film thickness, improving the electron mobility as observed.

Prediction of the thickness-dependent stability of PMMA columnar domains

As shown above, the most important factor that contributed to the improved charge transport properties and photovoltaic performance of ternary blend BHJ solar cells with increased optimal blend layer thickness is the presence of self-assembled vertical PMMA columnar domains within the blend film. By using molecular dynamics simulations, previously we could reproduce the spontaneous formation of PMMA columns and subsequent segregation of PCBM to the P3HT/PMMA interface in the ternary blend thin film.[37] Using the same approach, here we studied the structural stability of columnar PMMA domains and find that the PMMA columns become unstable as the blend film thickness increases, ultimately failing to extend vertically throughout the whole thickness.

For details, we used a bead-spring model to simulate the ternary blend film, where the system was confined between top and bottom surfaces. Since the PCBM is not interfering with the phase separation behavior of the two polymer components, we only focus on the interaction between the two polymers, each represented as Lennard-Jones (LJ) particles labelled as polymer A (non-photoactive) and polymer B (photoactive), with the number fractions of 20% and 80%, respectively. The interaction between the monomers was modeled with LJ potential U^{LJ}:

$$U^{LJ}(r) = 4\,\varepsilon\left[\left(\frac{\sigma}{r}\right)^{12} - \left(\frac{\sigma}{r}\right)^{6}\right] \qquad (2)$$

, where r is the inter-spacing between particles, σ is the characteristic distance at which the potential equals to zero for paired particles, and ε is the depth of the potential well, which is set to a unit value for the same type of polymers. The miscibility between the two polymers is controlled by varying from 0.5 to 1.0, where the smaller ε indicates a higher immiscibility (more details in Experimental section). The simulated thin film

thickness, z, was varied from 27σ to 43σ. The simulation shows that a continuous vertical columnar domain is stable for the whole surveyed thickness range when ε equals to 0.5 (Fig. 8). However, if the interfacial tension between the two polymers is decreased by increasing ε to 0.9, the columnar domain quickly becomes unstable with increasing film thickness; we find that the columnar domain is formed for small thicknesses ($z < \sim 27\sigma$) but becomes unstable and breaks down to metastable hemispherical domains if z increases beyond 29σ (see Fig. S4 in Supplementary information for the complete description of the critical film thickness at which the columnar structure breaks down, as a function of the interfacial tension). These results point that the *high interfacial energy* between the two polymeric components is important for stabilizing the columnar structure with increasing the ternary blend film thickness. Given the large immiscibility between P3HT and PMMA confirmed by the neutron reflectivity measurement, the simulation study well describes the observed spontaneous formation of PMMA columnar domains in the ternary BHJ blend thin film. In addition, the predicted instability of the column structure with increasing blend thin film thickness appears to coincide with the eventually decreasing, measured device photovoltaic performance in the ternary blend solar cells. Though a concrete conclusion warrants more structural characterization of thick ternary blend films, these data implicate that the phase stability of PMMA columnar domains could be also contributing to the observed thickness-dependence of ternary blend solar cell performance.

Conclusion

We have demonstrated that the photovoltaic performance of organic binary P3HT:PCBM BHJ blend could be improved by the addition of a tertiary PMMA phase via the spontaneous formation of columnar PMMA domains, resulting in the significantly increased optimal blend layer thickness. The systematic structural interrogation combining various complementary experimental measurements and molecular dynamics simulation showed that the high phase immiscibility between P3HT and PMMA was driving the self-assembly of vertical PMMA columnar domains, which induced the randomization of the P3HT lamellar domain orientation, alleviating the negative grain boundary effects on the hole transport through the P3HT phase. The PMMA columnar domain also resulted in the preferential segregation of PCBM at the P3HT/PMMA interface, improving the electron transport. The overall photovoltaic performance, including J_{SC} and PCE, of the ternary blend solar cells was improved accordingly compared with control binary blend devices, and more significantly, this enhancement was accompanied by the substantial increase in the optimal blend layer thickness over 300 nm, which should be highly useful for enabling the reliable large-area R2R-type organic solar cell fabrication. The identified rationale for the ternary blend BHJ structure has potentials to facilitate the reliable, practical large-area manufacturing of organic solar cells as well as the further improvement of organic

solar cell performance by, for instance, adding a photoactive tertiary polymer component of high phase immiscibility in binary BHJ blend solar cells.

Acknowledgements

This research was supported in part by NSF-1344267 program. This research was in part carried out at the Center for Functional Nanomaterials (CFN) of Brookhaven National Laboratory (BNL), which is supported by the U.S. Department of Energy, Office of Basic Energy Sciences, under Contract No. DE-SC0012704. We also would like to acknowledge the access to the ThINC facility at the Advanced Energy Center, Stony Brook University. We also thank Kim Kisslinger (BNL) for cross-sectional TEM experiments.

References

1 A. J. Heeger, *Adv. Mater.*, 2014, 26, 10-28.

2 G. Yu, J. Gao, J. C. Hummelen, F. Wudl and A. J. Heeger, *Science*, 1995, 270, 1789.

3 Y. Liu, C. C. Chen, Z. Hong, J. Gao, Y. M. Yang, H. Zhou, L. Dou, G. Li and Y. Yang, *Scientific reports*, 2013, 3, 3356.

4 L. Dou, J. You, J. Yang, C. C. Chen, Y. He, S. Murase, T. Moriarty, K. Emery, G. Li and Y. Yang, *Nat. Photon*., 2012, 6, 180-185.

5 D. H. Wang, A. K. K. Kyaw, J. R. Pouliot, M. Leclerc and A. J. Heeger, *Adv. Energy Mater*., 2014, 4, 1300835.

6 H. J. Park, M. G. Kang, S. H. Ahn and L. J. Guo, *Adv. Mater.*, 2010, 22, E247–E253.

7 X. Gu, Y. Zhou, K. Gu, T. Kurosawa, Y. Guo, Y. Li, H. Lin, B. C. Schroeder, H. Yan, F. Molina-Lopez and C. J. Tassone, *Adv. Energy Mater.*, 2017,

8 J. Alstrup, M. Jørgensen, A. J. Medford and F. C. Krebs, *ACS Appl. Mater. Interfaces, 2010, 2, 2819-2827.*

9 F. C. Krebs, Sol. Energ. Mat. Sol. Cells, 2009, 93, 394-412.

10 H. Hoppe and N. S. Sariciftci, *J. Mater*., 2004, 19, 1924-1945.

11 C. Winder and N. S. Sariciftci, *J. Mater. Chem*., 2004, 14, 1077-1086.

12 G. Li, V. Shrotriya, Y. Yao and Y. Yang, *J. Appl. Phys.*, 2005, 98, 043704.

13 M. O. Reese, A. J. Morfa, M. S. White, N. Kopidakis, S. E. Shaheen, G. Rumbles and D. S. Ginley, *Sol. Energy Mater. Sol. Cells*, 2008, 92, 746-752.

14 J. You, C. C. Chen, Z. Hong, K. Yoshimura, K. Ohya, R. Xu, S. Ye, J. Gao, G. Li and Y. Yang, *Adv. Mater*., 2013, 25, 3873-3978.

15 W. Yin and M. Dadmun, *ACS Nano*, 2011, 5, 4756-4768.

16 P. Schilinsky, C. Waldauf and C. J. Brabec, *Appl. Phys. Lett*., 2002, 81, 3885-3887.

17 B. A. Collins, J. R. Tumbleston and H. Ade, *J. Phys. Chem. Lett*., 2011, 2, 3135-3145.

18 W. Ma, C. Yang, X. Gong, K. Lee, and A. Heeger, *Adv. Funct. Mater*., 2005, 15, 1617-1622.

19 D. Chen, A. Nakahara, D. Wei, D. Nordlund and T. P. Russell, *Nano Lett*., 2011, 11, 561-567.

20 Y. Liang, Z. Xu, J. Xia, S.-T. Tsai, Y. Wu, G. Li, C. Ray and L. Yu, *Adv. Mater.*, 2010, 22, E135-E138.

21 J. S. Kim, Y. Park, D. Y. Lee, J. H. Lee, J. H. Park, J. K. Kim and K. Cho, *Adv. Funct. Mater*., 2010, 20, 540-545.

22 X. He, F. Gao, G. Tu, D. Hasko, S. Huttner, U. Steiner, N. C. Greenham, R. H. Friend and W. T. Huck, *Nano Lett.*, 2010, 10, 1302-1307.

23 F.-C. Chen, Y.-K. Lin and C.-J. Ko, *Appl. Phys. Lett.*, 2008, 92, 023307.

24 J. E. Allen, K. G. Yager, H. Hlaing, C.-Y. Nam, B. M. Ocko and C. T. Black, *Appl. Phys. Lett*., 2011, 99, 163301.

25 K. M. Coakley, B. S. Srinivasan, J. M. Ziebarth, C. Goh, Y. Liu and M. D. McGehee, *Adv. Funct. Mater*., 2005, 15, 1927-1932.

26 Y. Huang, W. Wen, S. Mukherjee, H. Ade, E. J. Kramer and G. C. Bazan, *Adv. Mater*., 2014, 26, 4168-4172.

27 Y. Kim, S. Cook, S. A. Choulis, J. Nelson, J. R. Durrant and D. D. C. Bradley, *Synth. Met.,2005, 152, 105-108.*

28 L. Lu, W. Chen, T. Xu and L. Yu, *Nat. Commun.,2015, 6, 7327.*

29 S.-Y. Chang, H.-C. Liao, Y.-T. Shao, Y.-M. Sung, S.-H. Hsu, C.-C. Ho, W.-F. Su and Y.-F. Chen, *J. Mater. Chem. A, 2013, 1, 2447-2452.*

30 Y. M. Yang, W. Chen, L. Dou, W.-H. Chang, H.-S. Duan, B. Bob, G. Li and Y. Yang, *Nat. Photon*., 2015, 9, 190-198.

31 L. Lu, T. Xu, W. Chen, E. S. Landry and L. Yu, *Nat. Photon*., 2014, 8, 716-722.

32 Y. C. Chen, C. Y. Hsu, R. Y. Y. Lin, K. C. Ho and J. T. Lin, *ChemSusChem*, 2013, 6, 20-35.

33 T. Goh, J.-S. Huang, B. Bartolome, M. Y. Sfeir, M. Vaisman, M. L. Lee and A. D. Taylor, *J. Mater. Chem. A*, 2015, 3, 18611-18621.

34 J.-S. Huang, T. Goh, X. Li, M. Y. Sfeir, E. A. Bielinski, S. Tomasulo, M. L. Lee, N. Hazari and A. D. Taylor, *Nat. Photon*., 2013, 7, 479-485.

35 B. M. Savoie, S. Dunaisky, T. J. Marks and M. A. Ratner, *Adv. Energy Mater*., 2015, 5, 1400891.

36 L. Yang, H. Zhou, S. C. Price and W. You, *J. Am. Chem. Soc., 2012, 134, 5432-5435.*

37 C. Pan, H. Li, B. Akgun, S. K. Satijia, Y. Zhu, D. Xu, J. Ortiz, D. Gersappe and M. H. Rafailovich, *Macromolecules*, 2013, 46, 1812-1819.

38 G. Krausch, E. J. Kramer, M. H. Rafailovich and J. Sokolov, *Appl. Phys. Lett*., 1994, 64, 2655-2657.

39 G. S. Grest and K. Kremer, *Phys. Rev*. A, 1986, 33, 3628.

40 K. Kremer and G. S. Grest, *J. Chem. Phys*., 1990, 92, 5057-5086.

41 S. H. Park, A. Roy, S. Beaupre, S. Cho, N. Coates, J. S. Moon, D. Moses, M. Leclerc, K. Lee and A. J. Heeger, *Nat. Photon*., 2009, 3, 297-302.

42 Y. M. Nam, J. Huh and W. H. Jo, *Sol. Energ. Mat. Sol. Cells*, 2010, 94, 1118-1124.

43 D. W. Sievers, V. Shrotriya and Y. Yang, *J. Appl. Phys.*, 2006, 100, 114509.

44 G. Dennler, M. C. Scharber and C. J. Brabec, *Adv. Mater*., 2009, 21, 1323-1338.

45 J. E. Allen and C. T. Black, *ACS Nano*, 2011, 5, 7986-7991.

46 C.-Y. Nam, Q. Wu, D. Su, C.-Y. Chiu, N. J. Tremblay, C. Nuckolls and C. T. Black, *J. Appl. Phys*., 2011, 110, 064307.

47 J. Zhao, A. Swinnen, G. V. Assche, J. Manca, D. Vanderzande and B. V. Mele, *J. Phys. Chem*., 2009, B 113, 1587-1591.

48 L. F. Drummy, R. J. Davis, D. L. Moore, M. Durstock, R. A. Vaia and J. W. Hsu, *Chem. Mater*., 2010, 23, 907-912.

49 L. G. Parratt, *Phys. Rev*., 1954, 95, 359.

50 A. J. Parnell, A. D. F. Dunbar, A. J. Pearson, P. A. Staniec, A. J. C. Dennison, H. Hamamatsu, M. W. A. Skoda, D. G. Lidzey and R. A. L. Jones, *Adv. Mater*., 2010, 22, 2444-2447.

51 J. W. Kiel, B. J. Kirby, C. F. Majkrzak, B. B. Maranville and M. E. Mackay, *Soft Matter*, 2010, 6, 641-646.

52 N. D. Treat, M. A. Brady, G. Smith, M. F. Toney, E. J. Kramer, C. J. Hawker and M. L. Chabinyc, *Adv. Energy Mater*., 2011, 1, 82-89.

53 M.-Y. Chiu, U. Jeng, C.-H. Su, K. S. Liang and K.-H. Wei, *Adv. Mater*., 2008, 20, 2573-2578.

54 E. D. Gomez, K. P. Barteau, H. Wang, M. F. Toney and Y.-L. Loo, *Chem. Commun*., 2011, 47, 436-438.

55 P. Kohn, Z. Rong, K. H. Scherer, A. Sepe, M. Sommer, P. Muller-Buschbaum, R. H. Friend, U. Steiner and S. Hüttner, *Macromolecules*, 2013, 46, 4002-4013.

56 E. Verploegen, R. Mondal, C. J. Bettinger, S. Sok, M. F. Toney and Z. Bao, *Adv. Funct. Mater*., 2010, 20, 3519-3529.

57 W.-R. Wu, U.-S. Jeng, C.-J. Su, K.-H. Wei, M.-S. Su, M.-Y. Chiu, C.-Y. Chen, W.-B. Su, C.-H. Su and A.-C. Su, *ACS Nano*, 2011, 5, 6233-6243.

58 V. D. Mihailetchi, H. Xie, B. de Boer, L. A. Koster and P. W. Blom, *Adv. Funct. Mater*., 2006, 16, 699-708.

59 T. Agostinelli, S. Lilliu, J. G. Labram, M. Campoy-Quiles, M. Hampton, E. Pires, J. Rawle, O. Bikondoa, D. D. Bradley, T. D. Anthopoulos and J. Nelson, *Adv. Funct. Mater*., 2011, 21, 1701-1708.

60 N. D. Treat, C. G. Shuttle, M. F. Toney, C. J. Hawker and M. L. Chabinyc, *J. Mater. Chem.*, 2011, 21, 15224-15231.

61 C.-Y. Nam, D. Su and C. T. Black, *Adv. Funct. Mater*., 2009, 19, 3552-3559.

62 X. Shen, V. V. Duzhko and T. P. Russell, *Adv. Energy Mater*., 2013, 3, 263-270.

63 I. Kang, H.-J. Yun, D. S. Chung, S.-K. Kwon and Y.-H. Kim, *J. Am. Chem. Soc*., 2013, 135, 14896-14899.

64 C.-W. Chu, H. Yang, W.-J. Hou, J. Huang, G. Li and Y. Yang, *Appl. Phys. Lett*., 2008, 92, 103306.

65 R. Street, J. Northrup and A. Salleo, *Phys. Rev. B*, 2005, 71, 165202.

66 L. H. Jimison, M. F. Toney, I. McCulloch, M. Heeney and A. Salleo, *Adv. Mater*., 2009, 21, 1568-1572.

67 R. J. Kline, M. D. McGehee, E. N. Kadnikova, J. Liu, J. M. Fréchet and M. F. Toney, *Macromolecules*, 2005, 38, 3312-3319.

68 H. Sirringhaus, P. Brown, R. Friend, M. M. Nielsen, K. Bechgaard, B. Langeveld-Voss, A. Spiering, R. A. Janssen, E. Meijer, P. Herwig and D. M. De Leeuw, *Nature*, 1999, 401, 685-688.

69 B. Walker, A. B. Tamayo, X.-D. Dang, P. Zalar, J. H. Seo, A. Garcia, M. Tantiwiwat and T.-Q. Nguyen, *Adv. Funct. Mater*., 2009, 19, 3063-3069.

70 G. Li, V. Shrotriya, J. Huang, Y. Yao, T. Moriarty, K. Emery, and Y. Yang, *Nat. Mater*. 2005, 4, 864-868.

71 S. S. Van Bavel, M. Bärenklau, G. de With, H. Hoppe and J. Loos, *Adv. Funct. Mater*., 2010, 20, 1458-1463.

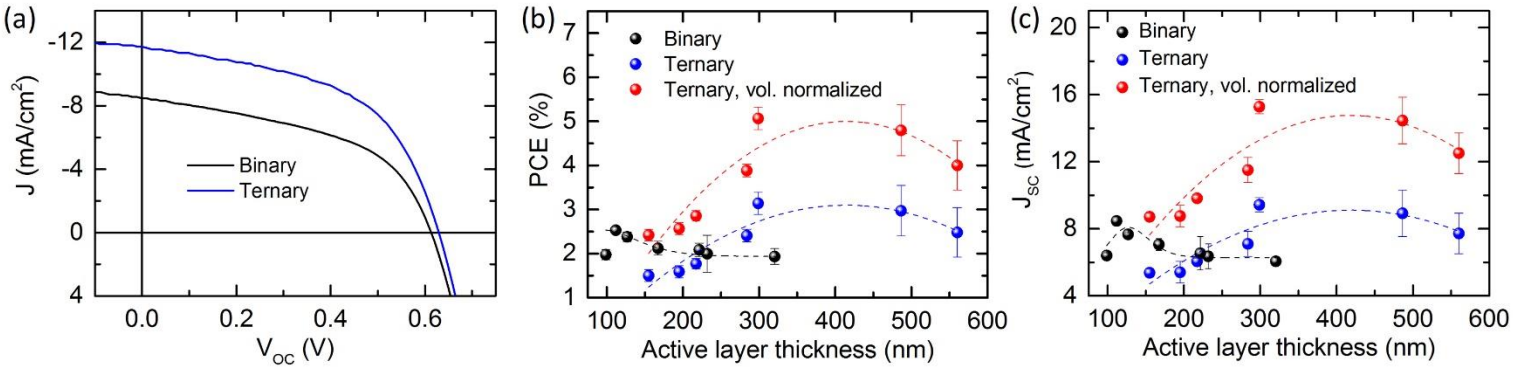

Fig. 1 (a) Representative J-V characteristics of champion P3HT:PCBM binary (black line) and P3HT:PMMA:PCBM ternary (blue line) BHJ blend solar cells measured under 1 Sun AM1.5G simulated solar illumination. (b) PCE vs. active layer thickness for binary blend (black sphere) and ternary blend (blue sphere) solar cells. Red spheres are for the ternary blend after normalizing by the photoactive blend volume. (c) J_{SC} vs. active layer thickness for binary blend (black sphere) and ternary blend (blue sphere) solar cells. Red spheres are for the ternary blend after normalizing by the photoactive blend volume. The dashed lines in (b) and (c) are guides to the eye only.

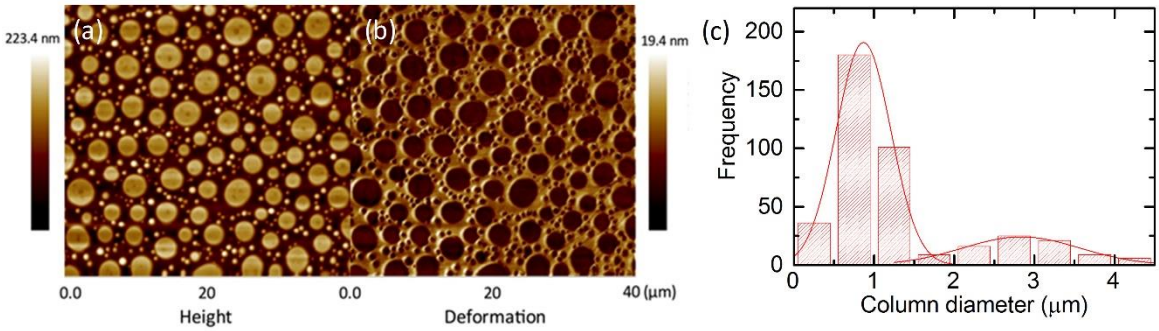

Fig. 2 AFM images of P3HT:PMMA:PCBM ternary BHJ blend thin film (1:1:1 wt. ratio, spin-cast on the PEDOT:PSS-coated ITO substrate, annealed at 150 °C for 1 hr in ~10 mTorr vacuum). (a) Topography (height) and (b) associated deformation (indentation depth) images, respectively. The scan size for all images is 40 μm × 40 μm. (c) Histogram showing the distribution of the diameters of circular domains obtained from (a). Solid lines denote Gaussian fits.

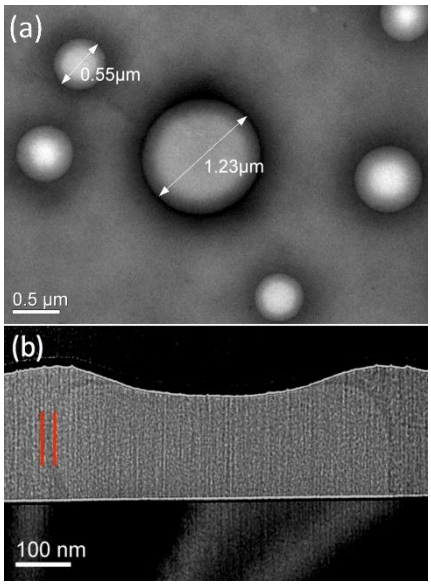

Fig. 3 (a) TEM image (top-view) of P3HT:PMMA:PCBM ternary blend thin film (1:1:1 wt. ratio, film floated off on a TEM grid and then annealed for 1 hr at 150 °C in ~10 mTorr vacuum). (b) Cross-sectional TEM image from the ternary blend thin film (identical blend condition as in (a), see Experimental section for the details of sample preparation). The width of marked region by two red solid lines is ~7 nm.

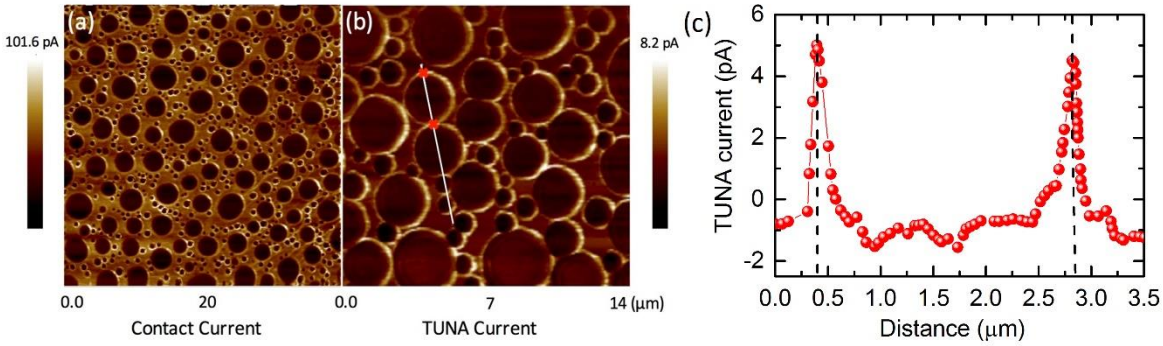

Fig. 4 PF-TUNA current images for the P3HT:PMMA:PCBM ternary blend (1:1:1 wt. ratio) thin films spin-cast on a Si or ITO substrate. The blend film was annealed at 150 °C for 1 hr in ~10 mTorr vacuum before the measurement. (a) Image of the ternary thin film spin-cast on a Si substrate, 40 μm × 40 μm scan size. (b) Higher resolution image of ternary thin film spin-coated on ITO substrate coated with 30 nm TiO_2 layer, 14 μm × 14 μm scan size. (c) TUNA current vs. distance profile along the line between two red dots marked in (b). It is noted that the TUNA current observed in (a) is substantially larger than (b) because the sample in (b) has TiO_2 bottom layer that acts as a hole-blocking contact while the TUNA current at the top surface is probed by a Au-coated AFM tip that primarily collects the hole current.

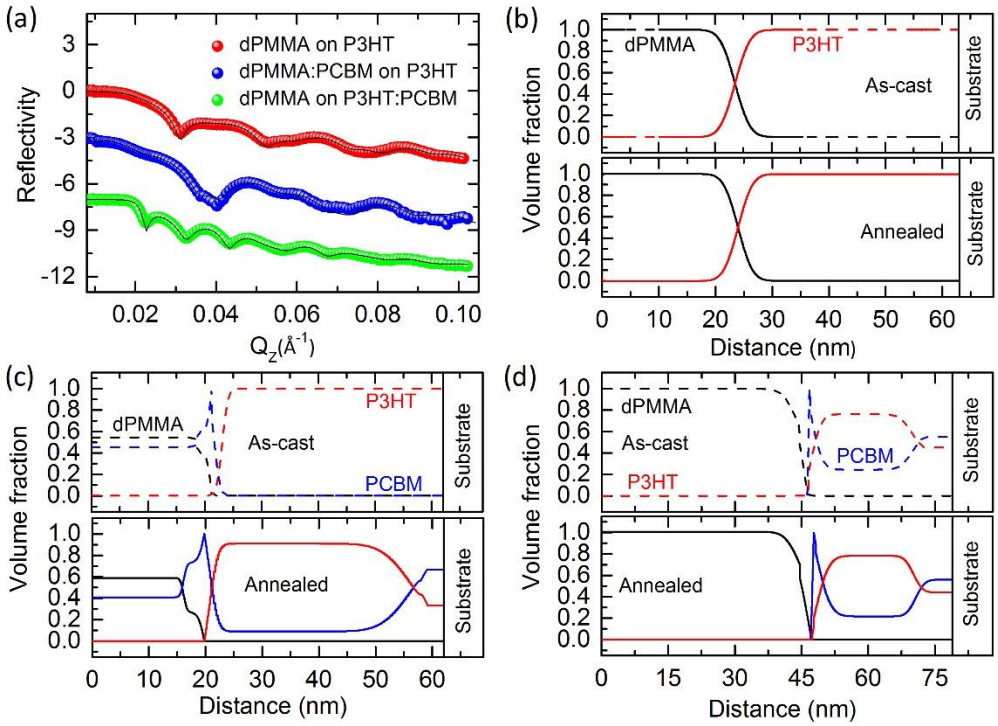

Fig. 5 (a) Representative measured neutron reflectivity profiles of control bilayer films after thermal annealing at 150 °C in ~10 mTorr vacuum: dPMMA/P3HT (red sphere), dPMMA:PCBM blend (50 wt.%)/P3HT (blue sphere), and dPMMA/P3HT:PCBM blend (50 wt.%) (green sphere) bilayers, respectively. (b)-(d) Volume fraction profiles extracted from the best fit results of neutron scattering data showing as-cast (dashed line, top panel) vs. after 90 min thermal annealing (solid lines, bottom panel) conditions: (b) dPMMA/P3HT, (c) dPMMA:PCBM blend (50 wt.%)/P3HT, and (d) dPMMA/P3HT:PCBM blend (50 wt.%) bilayers, respectively.

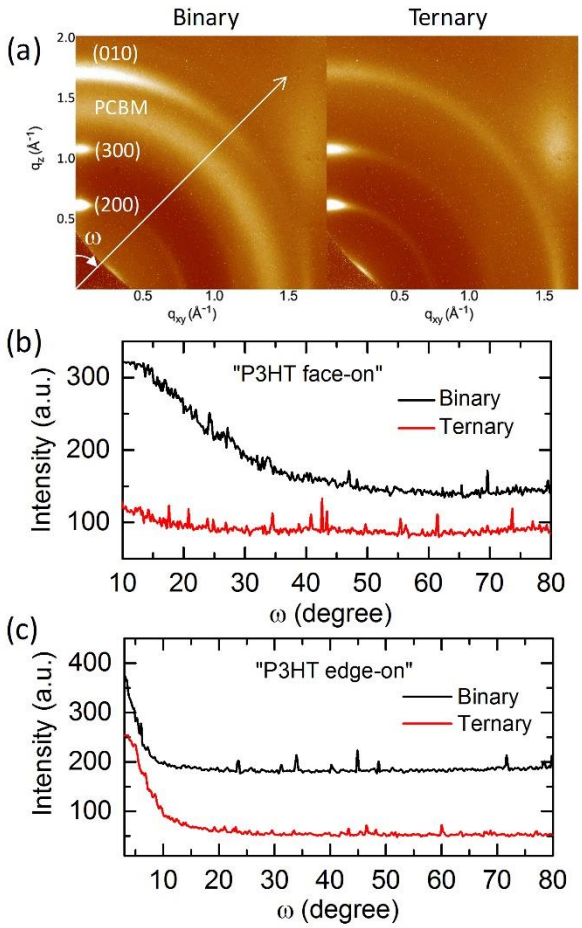

Fig. 6 (a) GIWAXS data, displaying two-dimensional distribution of X-ray scattering intensity from P3HT:PCBM binary blend (left panel) and P3HT:PMMA:PCBM ternary blend (right panel) thin films. (b) Angular distribution of the (010) face-on P3HT lamellar stacking peak (q = 1.71 Å^{-1}). (c) Angular distribution of the (300) edge-on P3HT lamellar stacking peak (q = 1.15 Å^{-1}).

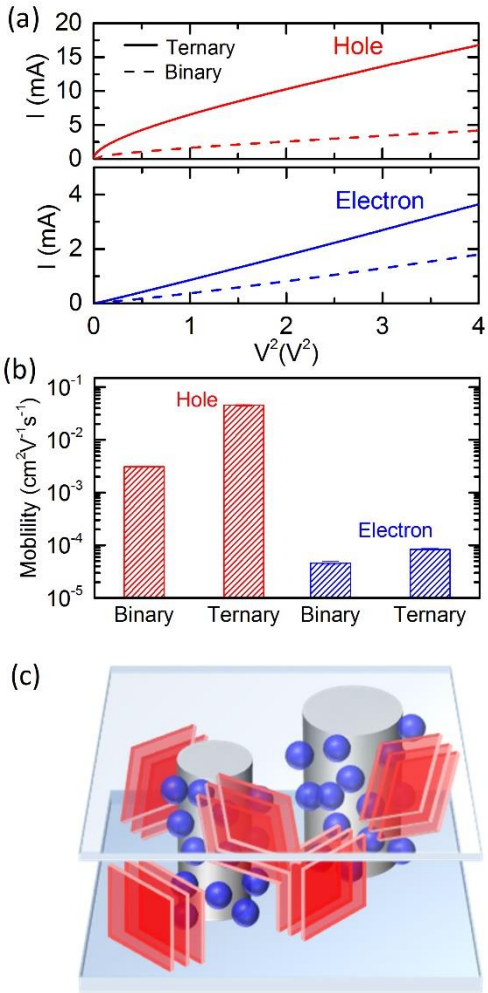

Fig. 7 (a) Representative measured I-V^2 characteristics for the hole-only (top panel) and electron-only (bottom panel) devices made from P3HT:PCBM binary (dashed lines) and P3HT:PMMA:PCBM ternary (solid lines) blend thin films. The linear portions of data were used to determine the slope and corresponding charge mobilities by SCLC model. (b) Histograms comparing hole and electron motilities obtained from P3HT:PCBM binary and P3HT:PMMA:PCBM ternary blend thin films. Average values are displayed (measured from five devices for each condition). (c) Schematic illustration of the internal structure of the P3HT:PMMA:PCBM ternary blend thin film. Stacked red rectangles represent P3HT lamellar domains, grey cylinders vertical PMMA columns, and blue spheres PCBM molecules.

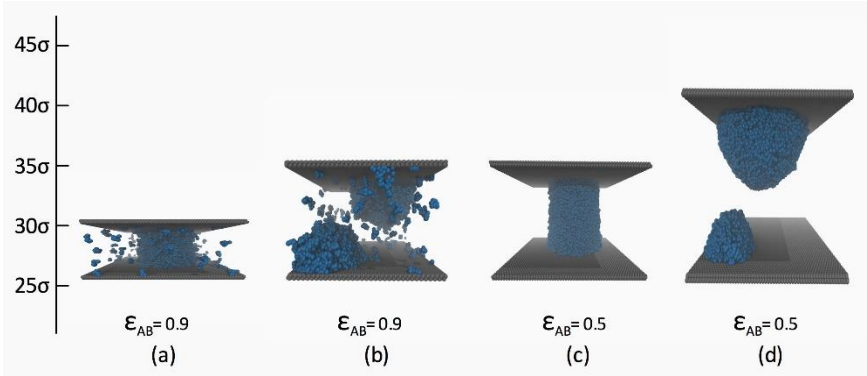

Fig. 8 Visualization of the internal morphology of a ternary blend thin film obtained by molecular dynamics simulation with different interfacial tensions and thicknesses. Since PCBM is not interfering with the phase separation of the two polymeric components in the ternary blend, it is not included in the simulation. The non-photoactive polymer component A is represented as a blue sphere, and the photoactive polymer component B occupies the rest of volume and is not displayed for clarity. Schematics show the morphologies obtained at: (a) $\varepsilon = 0.9$ and thickness of 31σ; (b) $\varepsilon = 0.9$ and thickness of 35σ; (c) $\varepsilon = 0.5$ and thickness of 35σ; and (d) $\varepsilon = 0.5$ and thickness of 43σ.

Table 1. Summary of champion device photovoltaic performance parameters in Fig. 1a

Blend condition	V_{oc} (V)	J_{sc} (mA/cm^2)	FF	PCE
Binary	0.605	8.47	49.4%	2.53%
Ternary	0.615	11.73	53.2%	3.84%

Table 2. Summary of average hole and electron mobilities measured by SCLC analysis for P3HT:PCBM binary and P3HT:PMMA:PCBM ternary blend thin films

Charge type	Mobility ($cm^2V^{-1}s^{-1}$)	
	Binary blend	Ternary blend
Hole	$3.1 \pm 0.24 \times 10^{-3}$	$4.5 \pm 0.2 \times 10^{-2}$
Electron	$4.6 \pm 0.35 \times 10^{-5}$	$8.4 \pm 0.35 \times 10^{-5}$

Table of content

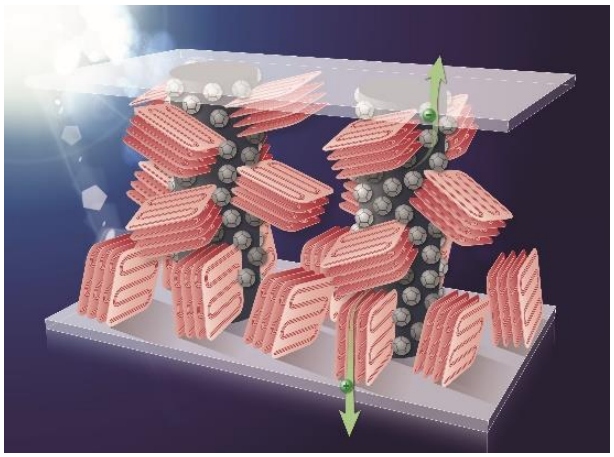

Self-assembled ternary blend bulk heterojunction increases the optimal blend thickness, making it suitable for practical roll-to-roll organic solar cell fabrication

Supplementary information

A new strategy to engineer polymer bulk heterojunction solar cells with thick active layers via self-assembly of columnar phase

Hongfei Li,[a] Zhenhua Yang,[a] Cheng Pan,[a] Naisheng Jiang,[a] Sushil K. Satija,[b] Di Xu,[a] Dilip Gersappe,[a] Chang-Yong Nam,[*,c] and Miriam H. Rafailovich [*a]

[a]Department of Materials Science and Engineering, Stony Brook University, Stony Brook, New York 11794, United States

[b]Center for Neutron Research, National Institute of Standards and Technology, Gaithersburg, Maryland 20899, United States.

[c]Center for Functional Nanomaterials, Brookhaven National Laboratory, Upton, New York 11973, United States

[*]E-mail: miriam.rafailovich@stonybrook.edu (M.H.R.), cynam@bnl.gov (C.-Y.N)

PCBM Weight Percentage Calculation

The weight fraction of PCBM (Φ) along the perimeter of the PMMA columns was calculated by using the following equation: $\Phi = \frac{V_c \rho_c}{V_t \rho_t}$, , where V_c is the volume of cylindrical shell of PCBM along the PMMA columns, ρ_c is the density of PCBM, V_t is the volume of active layer, ρ_t is the concentration of PCBM in the blend. We assume the PCBM aggregation layer along the PMMA columns as a cylindrical shell: $V_c = 2\pi r h \Delta$, where r is the column radius, h is the height of the cylindrical shell, Δr is the interfacial width of PCBM aggregation layer.

Domain Size Calculation by Scherrer Equation

The domain size of crystalline phase (e.g., P3HT, PCBM) can be calculated by the Scherrer equation using the full width at half maximum of a corresponding X-ray scattering peak: $d = \frac{0.9\lambda}{\beta \cos\theta}$, where d is the size of crystalline domain, λ is the X-ray wavelength, β is the full width at half maximum of a diffraction peak, and θ is the peak position.

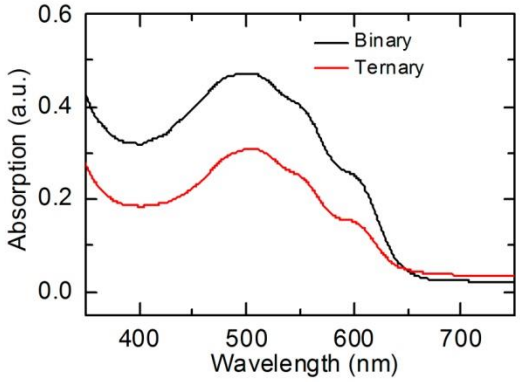

Fig. S1. Ultraviolet-visible light absorption spectra of ~210 nm thick thin film samples after thermal annealing at 150 °C for 1 hr in ~10 mTorr vacuum: P3HT:PMMA:PCBM ternary blend (red line); P3HT:PCBM binary blend (black line). The integrated absorption of the ternary blend in the measurement range is ~60% of that for the binary blend, which is consistent with the geometric volume fraction of photoactive P3HT:PCBM in the ternary blend sample.

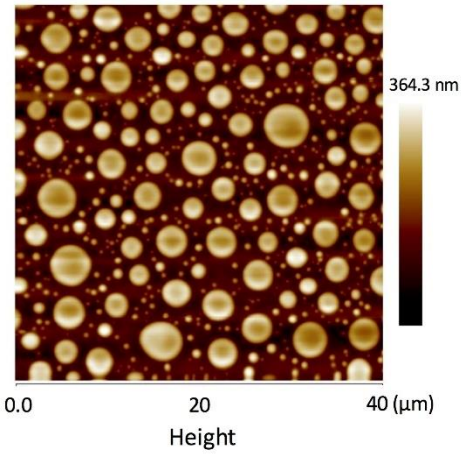

Fig. S2. Topographical AFM image of P3HT:PMMA:PCBM ternary BHJ blend thin film (1:1:1 wt. ratio, spin-cast on the PEDOT:PSS-coated ITO substrate, annealed at 150 °C for 1 hr in ~10 mTorr vacuum) *with top Al contact*. The scan size is 40 μm × 40 μm.

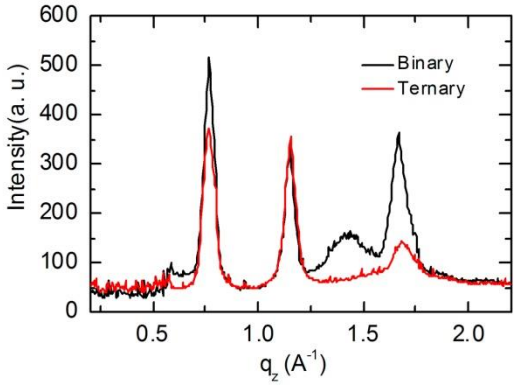

Fig. S3. Linear X-ray scattering intensity profile along the q_z axis obtained from the two-dimensional GIWAXS data measured from the binary P3HT:PCBM and ternary P3HT:PMMA:PCBM blend thin films prepared on Si. The films were annealed at 150 °C for 4 hr in ~10 mTorr vacuum before the measurement.

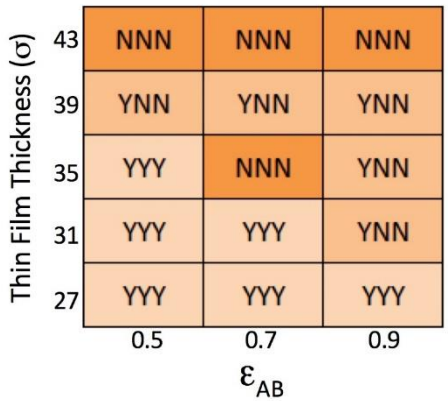

Fig. S4. Summary of percolating column structure formation for different simulation parameter settings. Three simulations were conducted for each combination of film thickness and ε. Y and N, respectively, denote the cases when percolating column structure is observed and not observed.

Table S1. Ternary blend solar cell photovoltaic parameters at different blend layer thicknesses

Thickness (nm)	V_{OC} (V)	J_{SC} (mA/cm^2)	FF	PCE
560.2 ± 2.55	0.615 ± 0.01	7.7247 ± 1.21	52.4 ± 0.8%	2.488 ± 0.56%
486.4 ± 2.35	0.625 ± 0.005	8.9235 ± 1.40	53.2 ± 1.1%	2.968 ± 0.57%
298.8 ± 1.42	0.625 ± 0.005	9.4326 ± 0.42	53.3 ± 1.3%	3.14 ± 0.25%
283.8 ± 1.14	0.615 ± 0.005	7.1042 ± 0.75	55.3 ± 0.6%	2.41 ± 0.15%
217.2 ± 0.75	0.615 ± 0.009	6.0629 ± 0.19	47.5 ± 1.8%	1.77 ± 0.12%
195.5 ± 0.64	0.615 ± 0.006	5.4106 ± 0.59	47.7 ± 1.9%	1.59 ± 0.14%
155.3 ± 0.51	0.615 ± 0.01	5.3796 ± 0.14	45.3 ± 1.6%	1.51 ± 0.13%

Table S2. Binary blend solar cell photovoltaic parameters at different blend layer thicknesses

Thickness (nm)	V_{OC} (V)	J_{SC} (mA/cm^2)	FF	PCE
320.4 ± 1.78	0.595 ± 0.01	6.0622 ± 0.25	53.6 ± 1.8%	1.934 ± 0.18%
231.8 ± 1.65	0.575 ± 0.02	6.3613 ± 0.74	54.3 ± 3.1%	1.989 ± 0.42%
221.4 ± 1.37	0.585 ± 0.005	6.5416 ± 0.99	54.1 ± 3.3%	2.069 ± 0.15%
167.2 ± 1.16	0.605 ± 0.005	7.0661 ± 0.36	50.1 ± 0.7%	2.1459 ± 0.16%
126.8 ± 0.55	0.605 ± 0.006	7.6671 ± 0.09	51.4 ± 1.4%	2.3860 ± 0.11%
111.8 ± 0.44	0.605 ± 0.005	8.4706 ± 0.24	49.4 ± 2.8%	2.5314 ± 0.08%
98.8 ± 0.31	0.595 ± 0.01	6.4094 ± 0.14	51.9 ± 1.7%	1.9791 ± 0.12%